nature communications

Article

https://doi.org/10.1038/s41467-025-64520-w

Link between cascade phenomenon and correlated Chern insulators in magic-angle twisted bilayer graphene

Received: 13 February 2025

Accepted: 18 September 2025

Published online: 28 October 2025

Check for updates

Qianying Hu[1,2,4], Shu Liang[3,4], Xinheng Li[2], Hao Shi[3], Xi Dai[3] & Yang Xu[1,2]

Chern insulators are topologically non-trivial states of matter characterized by incompressible bulk and chiral edge states. Incorporating topological Chern bands with strong electronic correlations provides a versatile playground for studying emergent quantum phenomena. In this study, we resolve the correlated Chern insulators (CCIs) satisfying $|\nu|+|C|=4$ in magic-angle twisted bilayer graphene (MATBG) through Rydberg exciton sensing and unveil their direct link with the zero-field cascade features in the electronic compressibility. The compressibility minima in the cascade are found to deviate substantially from nearby integer fillings (by $\Delta\nu$) and coincide with the onsets of CCIs in doping densities, yielding a quasi-universal relation $B_c=\Phi_O\Delta\nu/C$ (onset magnetic field B_c, magnetic flux quantumΦ_0 and Chern number C). We suggest these onsets lie on the intersection where the integer filling of localized "*f*-orbitals" and Chern bands are simultaneously reached. Our findings update the field-dependent phase diagram of MATBG and directly support the topological heavy fermion model.

Two-dimensional electronic systems hosting nontrivial Chern bands can give rise to the quantum anomalous Hall effect (QAHE) with spontaneous breaking of the time-reversal symmetry at zero magnetic fields[1–10]. However, in many systems such as the magnetic topological insulator $MnBi_2Te_4$[11,12], MATBG[13–22], and multilayer crystalline graphene[23–25], the Chern insulators ($C\neq0$) often need to be stabilized by a finite magnetic field. Understanding the driving force of this finite field is crucial for establishing unified theoretical frameworks. MATBG with multiple robust CCIs provides a good platform, where the CCIs in MATBG have been found to emanate from integer fillings ν of the moiré superlattice and follow the regular sequence of $(C, \nu) = (\pm3, \pm1)$, $(\pm2, \pm2)$, and $(\pm1, \pm3)$[13–22].

The nature of the ordered ground state at low temperatures is often closely related to its less ordered normal state at high temperatures, as exemplified by the link between superconductivity and strange metallicity in cuprates[26,27]. In MATBG, the interplay between spin, valley, and sublattice degrees of freedom, coupled with the helical Dirac electrons and narrow moiré bandwidth, creates a diverse ensemble of competing many-body ground states[28–31]. The normal states for the low-temperature correlated insulators and superconductivity are suggested to be "cascade of phase transitions", manifested as asymmetric sawtooth features commonly observed in the doping (n) dependences of the thermodynamic compressibility ($\partial n/\partial\mu$) or local spectroscopic measurements[20,28,29,32–36]. However, no consensus has been reached for these states. They transit to the CCIs under finite magnetic fields, while what governs the energy hierarchy and the critical magnetic fields (B_c) for these CCIs is poorly understood.

Here we report studies of twisted bilayer graphene (TBG) samples with $\theta=1.09°$-$1.25°$ close to the magic angle through Rydberg exciton

[1]Beijing National Laboratory for Condensed Matter Physics, Institute of Physics, Chinese Academy of Sciences, Beijing, China. [2]School of Physical Sciences, University of Chinese Academy of Sciences, Beijing, China. [3]New Cornerstone Science Laboratory, Department of Physics, Hong Kong University of Science and Technology, Clear Water Bay, SaiKung, NT, Hong Kong, China. [4]These authors contributed equally: Qianying Hu, Shu Liang. e-mail: daix@ust.hk; yang.xu@iphy.ac.cn

sensing[37–39]. The variation of thermodynamic compressibility of TBG with the filling factor ν and magnetic field B can be well captured. By carefully analyzing the results, we establish a straightforward link between the cascade phenomenon and the $|\nu|+|C|=4$ CCI series, i.e., the onset of the CCIs always aligns with the doping density where the electronic compressibility is minimized at zero magnetic fields. In other words, the ratio between $\Delta\nu$ and B_c equals a constant C/Φ_0. This observation extends across all six CCIs in MATBG and is discernible over a broader range of twist angles. The understanding of such experimental observations can be unified by the topological heavy fermion (THF) model. In AA-stacked sites, the integer filling of localized orbitals, known as "f-electrons", leads to the suppressed quasiparticle weight and enhanced local moments. Meanwhile, the remaining electrons, differentiated by $\Delta\nu$ and referred to as "c electrons", occupy AB-stacked sites from topological conduction bands and are responsible for the appearance of CCIs under magnetic fields. Our findings elucidate the intrinsic driving mechanism of the finite B_c, provide experimental evidence supporting the THF model[36,40–42], and offer a new perspective without considering any symmetry breaking on the physical origin of the cascade phenomenon.

Results

Sawtooth feature at $B=0$ and deviation from integer fillings

The device schematic is shown in Fig. 1a. A monolayer WSe_2 sensor is directly contacted to near-magic-angle TBG and encapsulated by hBN/graphite dielectrics where a gate voltage V_g is applied to tune the carrier density n in TBG. The optical detection has a spatial resolution of about 1 µm. In Fig. 1b, the doping-dependent reflectance contrast spectra of a 1.09° TBG/WSe_2 device are measured at a temperature $T=1.7$ K. The TBG barely has optical responses in this energy range and the main resonances arise from the WSe_2 excitons. The 1 s excitonic state (~1.70 eV) of the monolayer WSe_2 exhibits small variations while the 2 s resonance (~1.78 eV) features a sawtooth pattern ($|n|<3\times10^{12}\,cm^{-2}$), whose energy shift and intensity reflect the dynamic evolution of the electronic compressibility of TBG (refer to refs. 37–39 for details). For clarity, we present the color map of this region with its energy subtracted by a slowly varying smooth background as ΔE in Fig. 1c. The doping density is converted to the filling factor ν, the number of electrons ($\nu>0$) or holes ($\nu<0$) per moiré unit cell. The comprehensive data analyzing procedure is outlined in the Methods, and additional details can be found in Supplementary Fig. S1.

The thermodynamic ground state of the electronic phases in MATBG is mainly characterized by its compressibility $\partial n/\partial\mu$, which can be accessed by several experimental approaches including quantum capacitance[22], scanning electron transistor[16,20,32], and direct chemical potential (μ) measurements[34]. Indeed, the ΔE of the 2 s state distinctly mirrors the asymmetric sawtooth behavior in the direct measurement of inverse compressibility ($\partial\mu/\partial n$) of MATBG, thereby affirming the validity of our method. When MATBG enters the compressibility minimum, the dielectric screening effect on the 2 s exciton weakens, resulting in a peak in energy and enhanced spectral intensity for the 2 s exciton[39,43]. The zero-field sawtooth feature in the compressibility was initially interpreted as a cascade of phase transitions where the flavor (spin or valley) symmetry is spontaneously broken near the integer fillings[19,32]. However, direct evidence for symmetry breaking in the zero-field cascade phenomenon is lacking, and this concept is at odds with the observations that these states persist up to tens of Kelvin – a temperature comparable to the moiré bandwidth of approximately 10 meV[44,45].

Notably, in addition to the well-defined peaks at the $\nu=0$ charge-neutral point and the full-filling moiré superlattice gaps at $\nu=\pm4$, all six supplementary peaks around $\nu=\pm1$, ±2, ±3 deviate toward higher

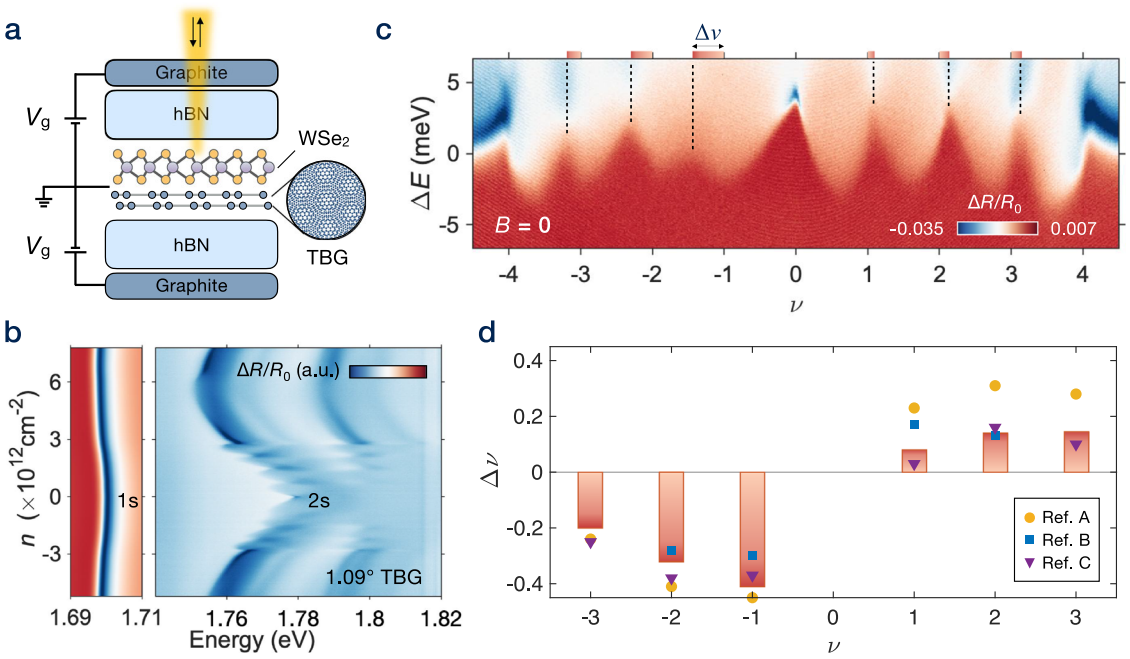

Fig. 1 | Optical detection of the zero-field compressibility evolution in 1.09° TBG. a Schematic illustration of the device structure and optical measurement. The TBG-WSe_2 is dual-gated by graphite-hBN dielectrics where the gate voltage V_g is applied. Optical detection of the compressibility evolution is facilitated through the Rydberg sensing scheme utilizing WSe_2 2 s excitons. **b** Doping dependence of the reflectance contrast spectra of the device. The sawtooth feature in the 2 s state originates from the nearly periodic changes in the electronic compressibility of TBG. **c** Magnified view of the sawtooth feature in the coordinate of ΔE (energy relative to a smooth baseline) and ν (moiré filling factor). The peaks at $\nu=\pm4$ align with the band insulator states, while those around $\nu=\pm1$, ±2, ±3 signify the other six compressibility minima that correspond to the cascade phenomenon. The red bars denote the deviation $\Delta\nu$ of the compressibility minima (indicated by dashed lines) from nearby integer fillings. **d** Deviation of the compressibility minima $\Delta\nu$ extracted from our work (bar) and previous compressibility measurements (symbols). Refs. A, B, and C are adapted from scanning electron transistor[32], quantum capacitance[22], and direct chemical potential[34] measurements, respectively.

https://doi.org/10.1038/s41467-025-64520-w

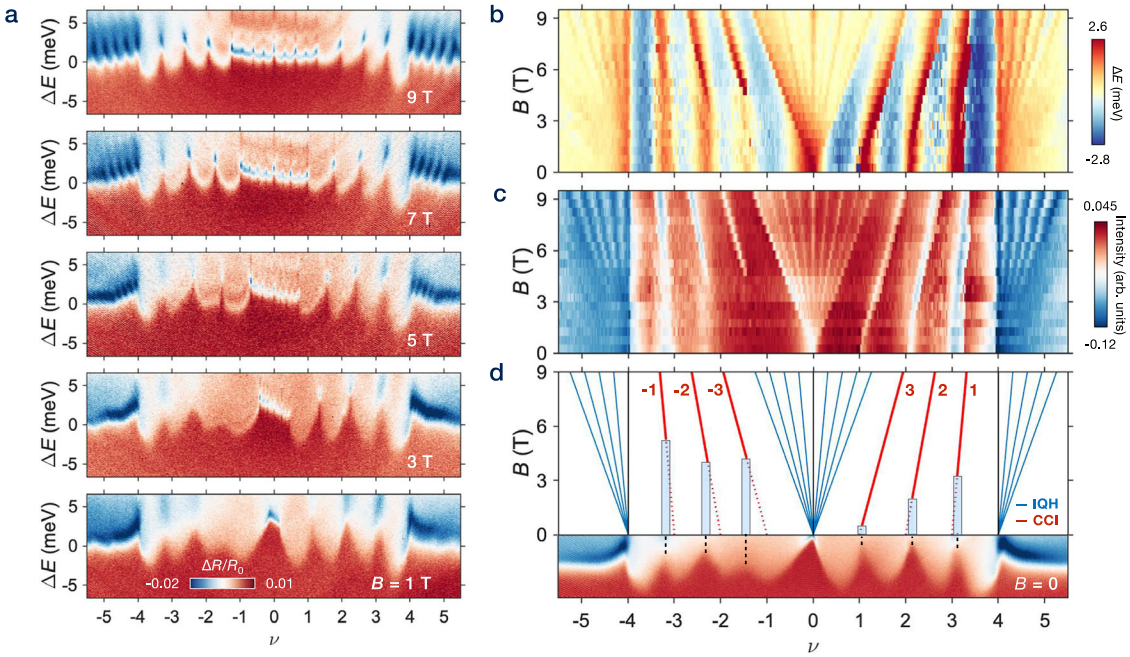

Fig. 2 | Correlated Chern insulators (CCIs) emerging at finite magnetic fields. **a** The spectral evolution of the sample under a perpendicular magnetic field. With increasing field strength, more peaks become identifiable and gradually shift in doping densities. Fan diagram constructed with the extracted energy ΔE (**b**) and intensity (**c**) of the 2 s state. Features with large ΔE and small intensity are associated with discernible states. **d** Schematics of the fan diagram (upper) and the spectrum in Fig. 1c for reference (lower). The integer quantum Hall (IQH) sequences originate from $\nu = 0$ and $\nu = \pm 4$, while the correlated Chern insulators (CCIs) emanate from $\nu = \pm 1, \pm 2, \pm 3$ (guided by the dashed lines) with their corresponding Chern numbers marked in red. As indicated by the blue bars, the onsets of the CCIs consistently occur at the doping density where the electronic compressibility is minimized at zero magnetic fields (marked by the vertical dashed lines).

density from nearby integer filling factors as indicated by the dashed lines and red bars. This deviation is also observed in many previous studies but has not yet been thoroughly analyzed or discussed[20,22,32,34]. We quantitively extract the deviation $\Delta\nu$ of compressibility minima from nearby integers in Fig. 1c. The values adapted from previous global[22,34] and local[32] compressibility measurements on MATBG are also shown in Fig. 1d. This deviation $\Delta\nu$ is discernible for all the six states, and is always positive on the electron side and negative on the hole side. Among different studies, the deviation in the hole doping side is more prominent than the electron doping side, whose absolute value can be as large as ~0.4 for the $\nu = -1$ state. The exact value shows slight variation between different studies, probably due to variations in the local strain or twist angles. This phenomenon extends beyond what could be attributed to experimental artifacts and may share the same origin with the resistance peak deviation from integers observed by several mesoscopic charge transport studies[21,34,35].

Correlated Chern insulators (CCIs) under finite magnetic fields

Following the zero-field measurements, we apply different perpendicular magnetic fields, and the spectral evolution is depicted in Fig. 2a. With increasing field strength, the single peak feature at $\nu = 0$ transforms into a cluster of peaks spanning a wider range in doping density, so are those at $\nu = \pm 4$. On the other hand, the peaks around $\nu = \pm 1, \pm 2, \pm 3$ become more defined after reaching a specific magnetic field strength and shift towards higher doping densities. In the top panel with $B = 9$ T, all the peaks are sharp in density and feature blue tails in energy, indicating the presence of incompressible gapped states.

As mentioned earlier, the evolution of compressibility in TBG manifests through two primary effects on the spectrum of Rydberg excitons: alterations in resonance energy and spectral intensity. To comprehensively examine the field-dependent evolution of these states, we extract these two values from the spectra (see details in Methods and Supplementary Fig. S1) and construct the fan diagrams presented in Fig. 2b, c. The fan diagrams extracted from ΔE and intensity exhibit similarities, and the topologically nontrivial gapped states originating from different integer moiré fillings are highlighted by the colored lines in Fig. 2d. They correspond to the integer quantum Hall states (IQH, guided by blue lines) with LL filling factors ν_{LL} and CCIs (guided by red lines) with Chern number C. Both ν_{LL} and C can be determined from the Streda formula $\Phi_0 dn/dB$ according to their slopes in the fan diagram.

Emanating from the charge neutrality point, the primary gapped states correspond to the empty/filled zeroth LL with $\nu_{LL} = \pm 4$ and the trivial gaps at $\nu_{LL} = 0$. All the other symmetry-broken quantum Hall ferromagnetic states at $0 < |\nu_{LL}| < 4$ are discernible at $B > -2$ T. Different experiments have revealed different sequences (being four-fold, two-fold, or single-fold degenerate) of the LLs originating from $\nu = 0$[13–22,46]. It is generally believed that the energy gaps are the strongest at $\nu_{LL} = \pm 4, \pm 2$, and 0, consistent with our observations. Additionally, two sets of fully degeneracy lifted LLs (with $\nu_{LL} = -4$ to -1 and 1 to 4, respectively) originate from the full filling gaps at $\nu = \pm 4$ after $B > -4$ T, and only the fans towards higher densities are retained.

In addition, six states labeled in red evolve from $\nu = \pm 1, \pm 2, \pm 3$ and become visible after reaching a certain critical magnetic field B_c, signifying the CCIs. It is typically understood that due to strong electronic interactions, the MATBG favors sequential fillings of the topologically nontrivial Hofstadter subbands with Chern numbers $C = -1$ for the holes and $C = 1$ for electrons[47]. Each Hofstadter subband is flavor polarized and corresponds to a single hole or electron occupying per moiré unit cell. This model can give the right sequence of Chern number C as a function of ν at the integer fillings, yielding $(C, \nu) = (\pm 3, \pm 1)$, $(\pm 2, \pm 2)$, and $(\pm 1, \pm 3)$. However, the certain value of the B field necessary to stabilize these CCIs in previous reports shows large variations without any universal pattern[13,14,18–20,22].

Here, we find the critical magnetic field B_c is determined by the deviation $\Delta\nu$ in the zero-field sawtooth feature. In Fig. 2d, the zero-field spectrum is placed beneath the fan diagram for reference. The peaks in the sawtooth feature consistently align with the CCI onsets. This

relation can be seen in the fan diagram in Fig. 2b, c where the onsets of the CCIs coincide with the vertical broader features that extend to zero magnetic field (indicated with blue bars in Fig. 2d). These features correspond to the low-field compressibility minima in the fan diagram, manifested as enhanced energies and oscillator strengths in the exciton resonance. It could be numerically expressed as $B_c = \Phi_0 \Delta\nu / C$ obtained from the slope of the CCIs following $\Delta\nu/B_c = dn/dB = C/\Phi_0$. The observed straightforward relationship applies well to all the six CCIs within the flat band, which suggests that the two independent topics mentioned earlier in this paper (the deviation of compressibility minima from integers in the cascade phenomenon & the critical B field of the CCIs) are strongly intertwined.

Link between cascade phenomenon and CCIs

To understand the identified link between the compressibility minimum and the emergence of CCIs, we first look back at the cascade phenomenon and consider their origins. The deviation of the compressibility minima from the nearby integer has two interesting features. First, the deviation only happens at non-zero integer fillings (±1, ±2, ±3). There is no deviation at all at the charge neutrality point (zero filling). Second, the deviation is positive on the electron side and is negative on the hole side, showing some approximate "particle-hole symmetry". Both two features can be well explained by the THF model for MATBG, where the flat bands can be decomposed into two different orbitals, the "f-orbitals" located at the AA stacking centers (majority, up to 95% of the flat bands) and the conduction "c-orbitals" distributed near the AB/BA stacking centers as illustrated in Fig. 3a.

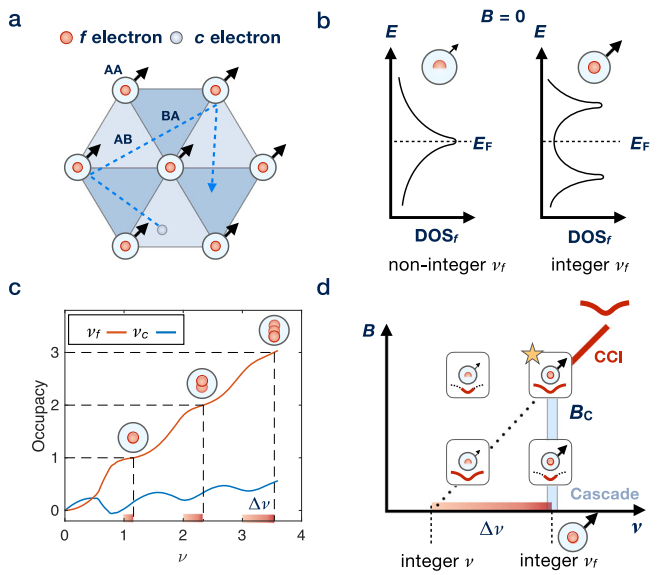

Fig. 3 | Topological heavy fermion (THF) picture for understanding the link between cascade phenomenon and CCIs. a Schematic illustration of the THF model with localized f-electrons (centered at AA stacking sites) serving as local moments (black arrow) and itinerant c electrons (centered at AB/BA stacking sites) with topological bands. **b** Schematics of the density of state suppression at integer ν_f. When the f-orbitals are occupied by integer electrons/holes, the suppression of the charge fluctuation on the f-orbitals and the electronic correlation becomes strongest, leading to a minimum in the local electronic density of state (DOS) and the enhanced local moments. **c** Calculated occupancy of the f- and c-orbitals upon electron filling. The integer filling of the f-orbitals ν_f naturally occurs at non-integer ν, and the deviation $\Delta\nu$ equals the filling of the conduction orbitals ν_c. **d** Schematics of the emergence of a correlated Chern insulators (CCI) state exemplified by the electron-doped side. Stabilizing CCI requires both a strong Hubbard interaction among the f-orbitals and the integer filling of Chern bands (schematically illustrated by the red curve). As a result, the CCIs emerge when the integer ν_f (blue bar) crosses the Streda line (dotted line), accounting for the observed link between cascade phenomenon and CCIs.

As discussed in references[41,48], the f-orbitals can be understood as the pseudo-Landau levels and are well localized near their centers. Therefore, the strongest Coulomb interaction U and correlation effects happen among those electrons occupying the f-orbitals, which capture the Mott physics in MATBG. On the other hand, the topological natures of the flat bands in MATBG can be well described by the non-trivial coupling terms between the f- and c- orbitals. Such a model with both localized and itinerant orbitals strongly mimics the heavy Fermion physics, where the strongly correlated physics, such as the Kondo effect, happens at the integer filling ν_f of the localized orbitals, rather than the integer filling ν of the entire system.

At zero field, when the filling factors of these f-orbitals (not the entire flat bands) ν_f reach integers, the strong correlation effects among the f-electrons will greatly suppress the charge fluctuations on the f-orbitals, and thus minimize quasi-particle weight and compressibility near the Fermi level as indicated in Fig. 3b (assuming no additional order in the ground states). Therefore, as the function of total filling factor ν, the local minima of compressibility should appear when the filling of the f-orbitals ν_f becomes integers, and the total filling factor ν will naturally be a non-integer with the deviation $\Delta\nu$ being the filling ν_c of those conduction orbitals at AB/BA stacking centers.

The above qualitative understanding is then confirmed by our numerical calculations based on the THF model for TBG using the Gutwiller variational method developed in ref. 49. As shown in Fig. 3c, the occupancy of f-orbitals ν_f shows a step-like character, while the c-orbitals are filled and depleted accordingly upon doping electrons. It would be symmetric on the hole side based on the THF model (see more discussions in Methods). The compressibility κ can be obtained by differentiating the occupation number respect to the total chemical potential directly (see Methods). The main results are shown in Supplementary Fig. S5, where we can see the minimum compressibility indeed happens around integer ν_f. Consequently, the experimentally observed cascade phenomenon can be utilized to determine the fillings of localized f-orbitals and itinerant c-orbitals. We note that in this picture, no symmetry breaking is involved to reproduce the experimentally observed cascade phenomenon, challenging previous claim of flavor symmetry-breaking phase transitions[20,32–36].

Under the finite magnetic field, the appearance of CCIs is closely related to the cascade phenomenon at zero field discussed in the previous section. A puzzling feature in the appearance of CCIs is that for nonzero fillings, only the CCIs with positive Chern numbers on the electron side and negative Chern numbers on the hole side have been detected. This can also be understood by considering the main driving force for stabilizing the symmetry-breaking states. First, the Hubbard interaction among the f-orbitals reaches a maximum at the integer ν_f. Second, the CCI can be formed only when the total filling of the system ν satisfies the Streda formula. Therefore, the CCI will be strongly favorable when these two conditions are both satisfied, as illustrated in Fig. 3d, which is only possible for the CCI with the positive (negative) Chern number on the electron (hole) side away from CNP.

Angle-dependent phase diagram

To further examine whether the observed link between the cascade phenomenon and the CCIs persists when the twist angle is slightly detuned from the magic-angle condition, we performed similar experiments on the sample with various twist angles and obtained the angle-dependent phase diagram.

Figure 4a–c presents the measured fan diagram and the corresponding zero-field spectra for regions with twist angles of 1.10°, 1.16°, and 1.18°, respectively. The comparison of these three fan diagrams vividly illustrates the evolution of the CCIs with twist angle (θ), and their onset magnetic fields B_c are summarized in Fig. 4d. The regions shaded in blue represent the CCI domes, determined by the measured B_c (filled triangles in blue) and the twist angle where the CCI is no

https://doi.org/10.1038/s41467-025-64520-w

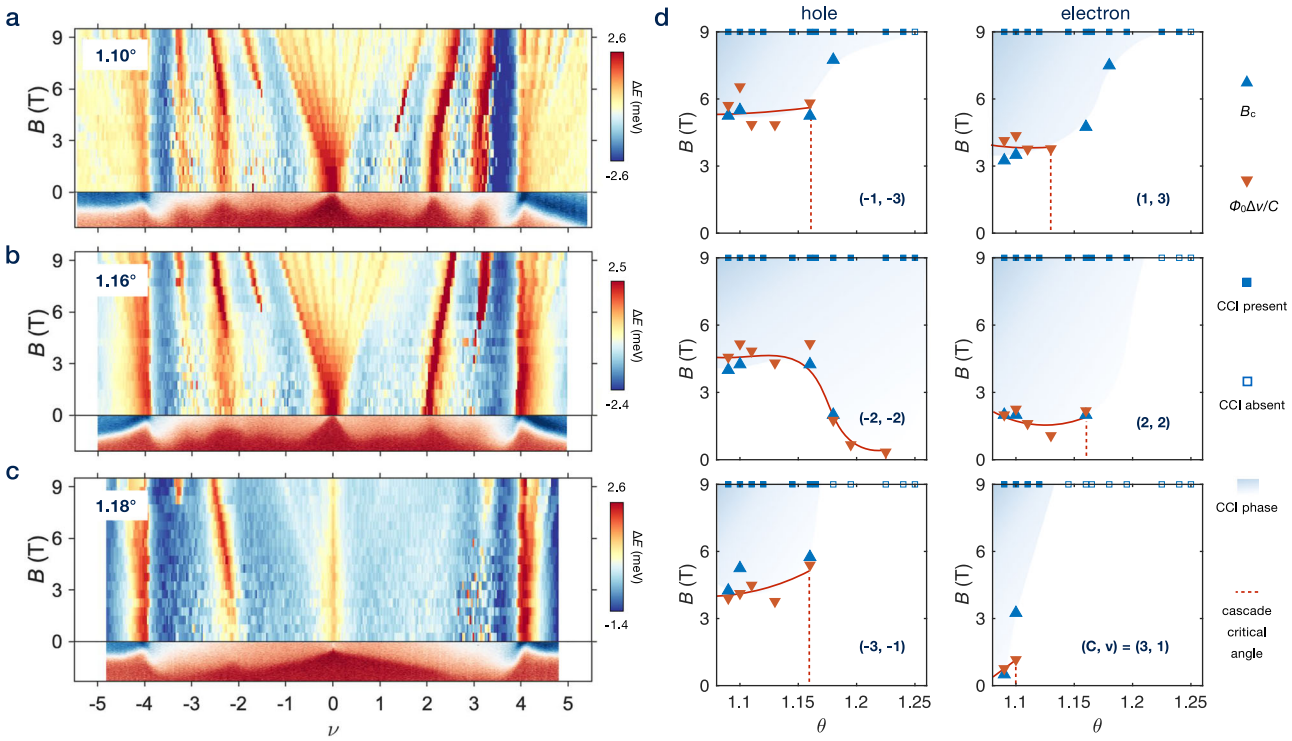

Fig. 4 | Angle-dependent phase diagram of the CCIs and their links with the zero-field spectra. a–c, Fan diagram (upper) and spectra at $B = 0$ (lower) of the 1.10° (**a**), 1.16° (**b**), and 1.18° (**c**) twisted samples. **d** Phase diagram of correlated Chern insulators (CCIs, shadowed blue regions) determined from B_c and the critical twist angle at $B = 9$ T. The CCI boundaries closely correspond to the zero field cascade features (guided by the red curves), highlighting the link between cascade phenomena and CCIs over a broader range detuned from the magic angle.

longer identifiable under $B = 9$ T (intersection between filled and empty squares in blue).

In our experiments, the twist angle ranges for almost all the CCIs are larger than previous reports[13–22,46]. This may be due to the sensitivity of the Rydberg sensing approach and/or the proximity-induced spin-orbit coupling effect by the adjacent WSe_2. Notably, the $(C, \nu) = (3, 1)$ state shows a minimal B_c of about 0.5 T for 1.09° TBG, whereas it increases rapidly as θ is slightly detuned, resulting in the most fragile CCI state against the twist angle. In contrast, some of the CCIs could survive in a much wider range such as the (±1, ±3) and (−2, −2) states, which are still observable up to 1.24° at $B = 9$ T, significantly beyond the magic angle. Moreover, one might intuitively expect that the stabilization of the CCIs needs a larger B_c when the twist angle deviates from the magic angle. However, the experimental data reveals a more intricate relationship as exemplified by the (−2, −2) state, where the B_c gets minimized when the twist angle is around 1.18°. These behaviors could stem from the multiple competing orders within the system, where minor variations in experimental conditions may prompt a shift to a different energetically favorable ground state.

We then turn our attention to the link between the cascade phenomenon and the CCIs. As depicted in Fig. 4a–c, for almost all the zero-field peaks in the lower panel, its filling factor aligns with the onset of CCIs. Another trend is that, at larger twist angles, some CCIs may not necessarily originate from a zero-field peak, such as the $(C, \nu) = (\pm1, \pm3)$ state for $\theta = 1.18°$. The peak feature is absent around $\nu = \pm3$ in the lower panel, while the corresponding CCIs still emerge at high magnetic fields. In Fig. 4d, we also plot the zero-field deviation $\Delta\nu$ multiplied by a constant Φ_0/C for samples with various twist angles near different integer fillings with red triangles. Red triangles are more abundant than the blue ones because they are extracted from faster zero-field measurements across a wider range of twist angles. The red dashed lines denote the largest angles where the cascade phenomenon exist, demonstrating their relatively narrower ranges of the twist angle compared to the CCIs. In such angle ranges, the values of B_c and $\Phi_0\Delta\nu/C$ exhibit a concurrence. It indicates the resilience of the relationship $B_c = \Phi_0\Delta\nu/C$ and the proposed mechanism across a broad spectrum of twist angles.

To summarize, we resolve the cascade phenomenon and $|\nu|+|C| = 4$ CCI series in MATBG through Rydberg exciton sensing and reveal their previously hidden link, which could be explained by the THF model. The cascade phenomenon manifested by asymmetric sawtooth features stems from the doping-dependent redistribution of charges between the localized *f*- and itinerant *c*- orbitals that does not require any symmetry breaking. Notably, both compressibility minima in the cascade phenomenon and the onsets of CCIs occur at integer fillings of the localized *f*-orbitals ν_f, rather than integer fillings of the entire system ν. Many puzzling experimental observations can now be well explained within this framework. For example, the finite B_c of CCIs is the natural result of the finite $\Delta\nu$ contributed by topological itinerant *c* electrons, hindering the observations of the QAHE in non-hBN aligned MATBG. Meanwhile, the non-diverging resistance peaks and the Pomeranchuk effect, which are both commonly found to occur at non-integer fillings of the entire system, are likely to arise from the suppression of the quasiparticle weight at integer ν_f and local moment fluctuations of *f*-orbitals at higher temperatures[21,34,35].

Methods

Device fabrication and electrostatic gating

The device fabrication process is identical to that described in our previous work[39] using the standard dry-transfer[50] and tear-and-stack[51] methods. The WSe_2, hBN, graphene, and few-layer graphite are mechanically exfoliated from bulk crystals and picked up layer by layer. The stack is released onto silicon substrates with pre-patterned gold electrodes, where the gate voltage V_g is symmetrically applied by Keithley 2400 source meters. The carrier density in TBG is calibrated by the spacing $n_0 = eB/h$ of the Landau level spectral features, where e

is the elementary charge. The twist angle is calculated from the full-filling density n_s at superlattice filling factor $\nu = \pm 4$ through $n_s \approx \frac{8\theta^2}{\sqrt{3}a^2}$(the graphene lattice constant $a = 0.246$ nm).

Reflectance spectroscopy measurements

The devices are measured in a close-cycle cryostat attoDry2100 at a base temperature of 1.7 K under a perpendicular magnetic field up to 9 T. The light source is a halogen lamp whose output is collected by a single-mode fiber and collimated by a ×10 objective lens. Magneto-optical measurements are performed with a circularly polarized light created by a linear polarizer and a quarter wave plate. A low-temperature compatible objective (NA = 0.82) focuses the beam onto the sample with a diameter of ~1 μm and a power lower than a few nW. The reflectance from the sample is collected by the same objective and detected by a spectrometer with 600 lines/mm gratings for fan-diagram measurements and 1800 lines/mm gratings for fine gate-dependent spectra measurements.

Background removal and extraction of energy and intensity

The optical measurement of TBG in this paper is based on the doping-dependent optical resonance of the 2 s Rydberg exciton. The reflectance contrast ($\Delta R/R_0$) spectrum is obtained by comparing the spectrum from the sample (R) with that from the substrate immediately next to the sample (R_0) as $\Delta R/R_0 = (R - R_0)/R_0$. The compressibility evolution of TBG will affect its energy and intensity in the gate-dependent $\Delta R/R_0$ spectrum. We aim to extract these two values properly and construct fan diagrams.

The raw data of the 1.09° device under $B = 0$ and $B = 9$ T are plotted in Supplementary Fig. S1a, d, respectively. We first subtract the background noise for more precise energy extraction in the next step (method described in ref. 39). By extracting the minima of $d(\Delta R/R_0)/dE$, we obtain and plot the absolute 2 s resonance energy in blue in these two figures. However, the absolute energy of the 2 s exciton upon doping is also affected by other issues beyond TBG compressibility, i.e., the spatial confinement of the exciton wave function by TBG moiré potential (formation of Rydberg moiré exciton). This effect is prominent in small-angle TBG devices as discussed in our previous work[39]. It is still not negligible in MATBG, manifesting as the non-monotonous energy shift upon doping in Fig. 1b.

To isolate the contribution from TBG compressibility evolution, we focus on the relative energy (ΔE) to the featureless baseline obtained by smoothing the extracted 2 s energy in this paper. As shown in Fig. S1b, e, the spectra after background subtraction are presented in the coordinate of ΔE. This region is between the yellow (7 meV lower than the baseline) and orange (7 meV higher than the baseline) curves in Supplementary Fig. S1a, d. The relative energy ΔE of the 2 s exciton (blue curves) is then used in the magnetic field-dependent counterplot in Fig. 2b. We extract the spectral intensity by integrating the $\Delta R/R_0$ in the region defined by blue and red lines in Supplementary Fig. S1b, e (~2 meV energy span). The integrated intensity is shown in Supplementary Fig. S1c, f, which is used to plot the fan diagram in Fig. 2c after normalization.

Method for calculation of no symmetry-breaking state

Single particle TB-model. The single particle Hamiltonian of TBG in each valley and spin can be described by 8 orbitals[52] (real-space distribution illustrated in Supplementary Fig. S4). They consist of two p± orbitals localized at AA point (f1: $p+$ @AA, f2: $p-$ @AA), a ring-shaped s orbital centered at AA point (c1: s @AA), a pair of p_z orbitals localized at AB and BA points (c2: p_z @AB, c3: p_z @BA), and three s orbitals localized at the three domain walls (c4: s @DW1, c5: s @DW2, c6: s @DW3). The first 2 orbitals are strongly correlated f orbitals (95% of flat bands), while the other 6 orbitals are weakly correlated c orbitals (5% of flat bands). The minimal tight-binding model we used for our calculation can be constructed faithfully within the twisted angle of 0.6°–1.3° [52]. The spread of the Wannier function of "f-orbitals" (AA_p orbitals in [52]) remains approximately unchanged for the twisted angle of 0.85°–1.3° as well as their intra-orbital Coulomb interaction strength [52]. As the angle reduces from 0.85° to 0.6°, the gap between flat bands and high energy dispersive bands gradually closes, resulting a larger hybridization between "f-orbitals" and "c-orbitals" [52], which would enhance the metallicity of the system, and the plateau in the "f-orbital" occupancy vs. total filling may vanish.

When considering the valley and spin degeneracy, we have $32 = 8(f) + 24(c)$ orbitals in total per unit cell. The effective TB Hamiltonian reads:

$$\hat{H}_0^{s\eta}(\boldsymbol{k}) = \sum_{tt'}^{1\sim2} \left[\mathcal{H}_{ff}^{\eta}(\boldsymbol{k})\right]_{tt'} f_{\boldsymbol{k}t\eta s}^{\dagger} f_{\boldsymbol{k}t'\eta s} + \sum_{aa'}^{1\sim6} \left[\mathcal{H}_{cc}^{\eta}(k)\right]_{aa'} c_{\boldsymbol{k}a\eta s}^{\dagger} c_{\boldsymbol{k}a'\eta s} + \sum_{t}^{1\sim2}\sum_{a}^{1\sim6} \left(\left[\mathcal{H}_{fc}^{\eta}(k)\right]_{ta} f_{\boldsymbol{k}t\eta s}^{\dagger} c_{\boldsymbol{k}a\eta s} + h.c.\right) \tag{1}$$

$$\hat{H}_0 = \sum_{\boldsymbol{k}s\eta} \hat{H}_0^{s\eta}(\boldsymbol{k}) \tag{2}$$

Where s and η denote spin and valley, t and a denote "f" and "c" orbitals, respectively.

Model Hamiltonian. The total Hamiltonian is written as:

$$\hat{H} = \hat{H}_0 + \hat{U} + \hat{W} + \hat{V} \tag{3}$$

$$\hat{U} = \frac{U}{2}\sum_{R}\sum_{\alpha\neq\beta}\left(\hat{n}_{Rf\alpha} - n_{Rf\alpha}^{CNP}\right)\left(\hat{n}_{\boldsymbol{R}f\beta} - n_{\boldsymbol{R}f\beta}^{CNP}\right) \tag{4}$$

$$\hat{W} = \mathrm{W}\sum_{\boldsymbol{R}}\sum_{\alpha\beta}\left(\hat{n}_{\boldsymbol{R}f\alpha} - n_{\boldsymbol{R}f\alpha}^{CNP}\right)\left(\hat{n}_{\boldsymbol{R}c\beta} - n_{\boldsymbol{R}c\beta}^{CNP}\right) \tag{5}$$

$$\hat{V} = \frac{V}{2}\sum_{\boldsymbol{R}}\sum_{\alpha\neq\beta}\left(\hat{n}_{\boldsymbol{R}c\alpha} - n_{\boldsymbol{R}c\alpha}^{CNP}\right)\left(\hat{n}_{\boldsymbol{R}c\beta} - n_{\boldsymbol{R}c\beta}^{CNP}\right) \tag{6}$$

Here $\hat{U}, \hat{W}, \hat{V}$ are the onsite interaction among "f-orbitals", effective interaction between "f-orbitals" and "c-orbitals", and effective interaction among "c-orbitals", respectively. The $\hat{U}$ is treated with Gutzwiller approximation while $\hat{W}, \hat{V}$ are treated at Hartree level in our calculation (specified below). The α, β are combined indices of spin, valley, and orbitals. The R marks the moiré unit cell. Double countings are considered within $\hat{U}, \hat{W}, \hat{V}$ by subsracting density operator with its occupation value at charge neutrality point (CNP). The interaction parameters used in this work are: $U = 0.08$eV, $W = 0.07$eV, $V = 0.07$eV. Here $\hat{W}, \hat{V}$ are effective interactions in the sense that they are approximations of realistic nearest neighbor interaction involving "c-orbitals" which makes W and V become many times larger than actually calculated values[36]. In addition, the effective $\hat{W}, \hat{V}$ won't break any symmetry here since they're treated at Hartree level. We adopt such approximation because we identify $\hat{U}$ as our primary contribution to the correlated effect in this system and we would like to reduce the total number of parameters.

Gutzwiller variational scheme. First we introduce the Gutzwiller correlator[49,53,54] for site $\boldsymbol{R}$:

$$\hat{P}_{\boldsymbol{R}} = \sum_{I} \lambda_{\boldsymbol{R};I} |\boldsymbol{R}; I\rangle\langle\boldsymbol{R}; I| \tag{7}$$

Where $\lambda_{\boldsymbol{R};I}$ is the variational parameter, $|\boldsymbol{R}; I\rangle$ is many-body Fock state consisting of local "f-orbitals" and $|\boldsymbol{R}; I\rangle\langle\boldsymbol{R}; I|$ is a projector which projects out states other than $|\boldsymbol{R}; I\rangle$ (We'll use α as integrated indices

for $s\otimes\eta\otimes t$ in this section):

$$|\boldsymbol{R};\boldsymbol{I}\rangle=\prod_{\alpha\in\boldsymbol{I}}\hat{f}_{\boldsymbol{R};\alpha}{}^{\dagger}|vaccum\rangle \tag{8}$$

$$|\boldsymbol{R};\boldsymbol{I}\rangle\langle\boldsymbol{R};\boldsymbol{I}|=\prod_{\alpha\in\boldsymbol{I}}\hat{n}_{\boldsymbol{R};f\alpha}\prod_{\beta\notin\boldsymbol{I}}\left(1-\hat{n}_{\boldsymbol{R};f\beta}\right) \tag{9}$$

Here, we use a diagonal $\hat{P}_{\boldsymbol{R}}$ because only density-density interaction is included. The Gutzwiller variational wavefunction is obtained by acting $\hat{P}_{\boldsymbol{R}}$ on a trial non-interacting Fermi Sea $|\Phi_0\rangle$:

$$|\Psi_G\rangle=\prod_{\boldsymbol{R}}\hat{P}_{\boldsymbol{R}}|\Phi_0\rangle \tag{10}$$

Gutzwiller approximation puts some constraints on λ_I:[53,55]

$$\langle\Phi_0|\hat{P}_R^2|\Phi_0\rangle=1 \tag{11}$$

$$\langle\Phi_0|\hat{P}_{\boldsymbol{R}}^2\hat{n}_{\boldsymbol{R}f\alpha}|\Phi_0\rangle=\langle\Phi_0|\hat{n}_{\boldsymbol{R}f\alpha}|\Phi_0\rangle \tag{12}$$

The total energy is then (N_m: number of unit cells or k points):

$$E_{total}=\frac{1}{N_m}\left\langle\Psi_G,|,\hat{H}_0+\hat{U}+\hat{W}+\hat{V}|\Psi_G\right\rangle \tag{13}$$

The first term is the kinetic energy (we denote $\left\langle\hat{O}\right\rangle_0=\langle\Phi_0|\hat{O}|\Phi_0\rangle$):

$$\begin{aligned}E_{kin}=&\frac{1}{N_m}\sum_{\boldsymbol{ks\eta}}\sum_{\mathrm{tt'}}^{1\sim2}\left[\mathcal{H}_{ff}^{\eta}(\boldsymbol{k})\right]_{\mathrm{tt'}}\mathcal{Z}_{t\eta s}\left\langle f_{\boldsymbol{k}t\eta s}^{\dagger}f_{\boldsymbol{k}t'\eta s}\right\rangle_0\mathcal{Z}_{t'\eta s}\\&+\frac{1}{N_m}\sum_{\boldsymbol{ks\eta}}\sum_{aa'}^{1\sim6}\left[\mathcal{H}_{cc}^{\eta}(\boldsymbol{k})\right]_{aa'}\left\langle c_{\boldsymbol{k}a\eta s}^{\dagger}c_{\boldsymbol{k}a'\eta s}\right\rangle_0\\&+\sum_{\mathrm{t}}^{1\sim2}\sum_{a}^{1\sim6}\left(\left[\mathcal{H}_{fc}^{\eta}(\boldsymbol{k})\right]_{\mathrm{t}a}\mathcal{Z}_{t\eta s}\left\langle f_{\boldsymbol{k}t\eta s}^{\dagger}c_{\boldsymbol{k}a\eta s}\right\rangle_0+h.c.\right)\end{aligned} \tag{14}$$

Where $\mathcal{Z}_\alpha$ is the renormalization factor (the site index $\boldsymbol{R}$ is omitted from now; $n_{\mathrm{f}\alpha}^0=\left\langle\hat{n}_{\boldsymbol{R}f\alpha}\right\rangle_0$):

$$\mathcal{Z}_\alpha=\lambda^{\top}\mathbb{R}_\alpha\lambda \tag{15}$$

$$(\mathbb{R}_\alpha)_{II'}=\frac{1}{2}\sqrt{\frac{m_I^0m_{I'}^0}{n_{\mathrm{f}\alpha}^0(1-n_{\mathrm{f}\alpha}^0)}}(\delta_{I,I'\cup\alpha}+\delta_{I\cup\alpha,I'}) \tag{16}$$

$$m_I^0=\prod_{\alpha\in I}n_{\mathrm{f}\alpha}^0\prod_{\beta\notin I}\left(1-n_{\mathrm{f}\beta}^0\right) \tag{17}$$

The second term is the interaction energy among "f-orbitals":

$$E_{\mathrm{int}}^{ff}=\lambda\mathbb{H}_{\mathrm{int}}\mathbb{m}^0\lambda-U\sum_{\alpha\neq\beta}n_{f\alpha}^0n_{f\beta}^{CNP}+\frac{U}{2}\sum_{\alpha\neq\beta}n_{f\alpha}^{CNP}n_{f\beta}^{CNP} \tag{18}$$

$$(\mathbb{H}_{\mathrm{int}})_{II'}=\delta_{II'}\frac{U}{2}\left\langle I\left|\sum_{\alpha\neq\beta}\hat{n}_{f\alpha}\hat{n}_{f\beta}\right|I\right\rangle \tag{19}$$

$$(\mathbb{m}^0)_{II'}=\delta_{II'}m_I^0 \tag{20}$$

Since $\hat{P}_{\boldsymbol{R}}$ does not contain "c-orbitals", $\left\langle\Psi_G,|,\hat{W}+\hat{V}|\Psi_G\right\rangle=\left\langle\Phi_0,|,\hat{W}+\hat{V}|\Phi_0\right\rangle$ under Gutzwiller approximation. Using Hartree approximation for these 2 terms:

$$\langle\Phi_0|\hat{W}|\Phi_0\rangle=W\left(n_f^0-n_f^{CNP}\right)\left(n_c^0-n_c^{CNP}\right) \tag{21}$$

$$\langle\Phi_0|\hat{V}|\Phi_0\rangle\approx\frac{V}{2}\left(n_c^0-n_c^{CNP}\right)\left(n_c^0-n_c^{CNP}\right) \tag{22}$$

Here we denote $n_f^0=\sum_\alpha n_{f\alpha}^0$ and $n_c^0=\sum_\beta n_{c\beta}^0$. Notice that we dropped the self-energy in $\langle\Phi_0|\hat{V}|\Phi_0\rangle$ since we want to reduce the number of variables in the final energy functional (using the total occupancy of "c-orbitals" instead of their individual occupancies, which will become clear in the following text).

We use an efficient variational scheme developed in ref. 49, where orbital occupancies are input variables for the energy functional. Since were considering a no-symmetry breaking state, only the total occupancy n_f (denoted as ν_f in the main text) matters for f-orbitals as $n_{f\alpha}=\frac{n_f}{8}$. To reduce the number of total variables in the energy functional, we only consider the total occupancy for c-orbitals n_c (denoted as ν_c in the main text). The energy functional $E_G=E_{total}$ when variational constraints are satisfied:

$$\begin{aligned}E_G\left(n_f,n_c\right)=&\frac{1}{N_m}\left\langle\Psi_G|\hat{H}_0+\hat{U}|\Psi_G\right\rangle+W\left(n_f-n_f^{CNP}\right)\left(n_c-n_c^{CNP}\right)\\&+\frac{V}{2}\left(n_c-n_c^{CNP}\right)\left(n_c-n_c^{CNP}\right)+\sum_\alpha\lambda_{\mathrm{f}\alpha}^{\mathrm{F}}\left(\left\langle\hat{n}_{\boldsymbol{R}f\alpha}\right\rangle_0-\frac{n_f}{8}\right)\\&+\lambda_{\mathrm{c}}^{\mathrm{F}}\left(\sum_\beta\left\langle\hat{n}_{\boldsymbol{R}c\beta}\right\rangle_0-n_c\right)+\sum_\alpha\lambda_{\mathrm{f}\alpha}^{\mathrm{B}}\left(\sum_{\alpha\in\mathrm{I}}\lambda_I^2m_I^0-\frac{n_f}{8}\right)\\&+E^F\left(1-\langle\Phi_0|\Phi_0\rangle\right)+E^B\left(1-\sum_{\mathrm{I}}\lambda_I^2m_I^0\right)\end{aligned} \tag{23}$$

Where $\lambda^F,\lambda^B,E^F,E^B$ are Lagrange multipliers for constraints on $|\Phi_0\rangle$ and $\boldsymbol{\lambda}$. Given a set of (n_f,n_c), we treat $|\Phi_0\rangle$ and λ as independent variables which should minimize $E_G|_{n_f,n_c}$:

$$\frac{\delta E_G}{\delta\langle\Phi_0|}|_{n_f,n_c,\lambda}=0\rightarrow\hat{H}^F|\Phi_0\rangle=\mathrm{E}^{\mathrm{F}}|\Phi_0\rangle \tag{24}$$

$$\frac{\delta E_G}{\delta\lambda}|_{n_f,n_c,|\boldsymbol{\Phi_0}\rangle}=0\rightarrow\hat{H}^B\lambda=E^B\mathbb{m}^0\lambda \tag{25}$$

$$\begin{aligned}\hat{H}^F=\sum_{ks\eta}\Bigg\{&\sum_{\mathrm{tt'}}^{1\sim2}\left[\mathcal{H}_{ff}^{\eta}(\boldsymbol{k})\right]_{\mathrm{tt'}}\mathcal{Z}_{t\eta s}f_{\boldsymbol{k}t\eta s}^{\dagger}f_{\boldsymbol{k}t'\eta s}\mathcal{Z}_{t'\eta s}+\sum_{aa'}^{1\sim6}\\&\left[\mathcal{H}_{cc}^{\eta}(\boldsymbol{k})\right]_{aa'}c_{\boldsymbol{k}a\eta s}^{\dagger}c_{\boldsymbol{k}a'\eta s}+\sum_{\mathrm{t}}^{1\sim2}\sum_{a}^{1\sim6}\left(\left[\mathcal{H}_{fc}^{\eta}(\boldsymbol{k})\right]_{\mathrm{t}a}\mathcal{Z}_{t\eta s}f_{\boldsymbol{k}t\eta s}^{\dagger}c_{\boldsymbol{k}a\eta s}+h.c.\right)\\&+\sum_{t}^{1\sim2}\lambda_{\mathrm{f};t\eta s}^{\mathrm{F}}\hat{n}_{f;\boldsymbol{k}t\eta s}+\lambda_{\mathrm{c}}^{\mathrm{F}}\left(\sum_{a}^{1\sim6}\hat{n}_{c;\boldsymbol{k}a\eta s}\right)\Bigg\}\end{aligned} \tag{26}$$

$$\hat{H}^B=\sum_\alpha\chi_\alpha\mathbb{R}_\alpha+\mathbb{H}_{\mathrm{int}}\mathbb{m}^0+\sum_\alpha\lambda_{\mathrm{f}\alpha}^{\mathrm{B}}\mathbb{N}_\alpha\mathbb{m}^0 \tag{27}$$

$$\begin{aligned}\chi_\alpha=&\frac{2}{N_m}\sum_{\boldsymbol{ks\eta}}\sum_{\mathrm{tt'}}^{1\sim2}\left[\mathcal{H}_{ff}^{\eta}(\boldsymbol{k})\right]_{\mathrm{tt'}}\left\langle f_{\boldsymbol{k}t\eta s}^{\dagger}f_{\boldsymbol{k}t'\eta s}\right\rangle_0\mathcal{Z}_{t'\eta s}\\&+\sum_{\mathrm{t}}^{1\sim2}\sum_{a}^{1\sim6}\left(\left[\mathcal{H}_{fc}^{\eta}(\boldsymbol{k})\right]_{\mathrm{t}a}\left\langle f_{\boldsymbol{k}t\eta s}^{\dagger}c_{\boldsymbol{k}a\eta s}\right\rangle_0+h.c.\right)(\mathbb{N}_\alpha)_{II'}=\left\langle I\left|\hat{n}_{f\alpha}\right|I'\right\rangle\end{aligned} \tag{28}$$

$\min E_G|_{\mathrm{n_f,n_c}}$ can be found by solving the 2 linear Eqs. (24) and (25) self-consistently. The solution of (24) gives us χ_α, which serves as input

for (25). Conversely, the solution of (25) gives us $\mathcal{Z}_\alpha$, which serves as input for (24).

Given an electron filling ν, we have $n_f + n_c = \nu$. The inverse compressibility $\kappa^{-1} = \frac{\partial^2 \min E_G}{\partial \nu^2}$ is calculated numerically. The presented result for inverse compressibility is smoothed to compensate numerical errors. We note that the THF model is particle-hole symmetric [40] and the minimal TB model we used possesses an approximate particle-hole symmetry [52]. The doping-dependent redistribution of charges between the localized *f*- and itinerant *c*- orbitals is a result of our calculation, which is performed on a fully-symmetric state with a particle-hole symmetric interaction Hamiltonian. Therefore, the *f*-*c* orbital charge redistribution is also particle-hole symmetric in our calculation. We hence only performed calculations in the electron-doped side (Fig. 3c and Supplementary Fig. S5). In order to capture the asymmetric behavior of electron and hole sides observed in experiments, one may need to consider symmetry breaking phases in their calculation (For example, breaking $C_{2z}T$ symmetry). In Fig. 3c, the calculated ν_c becomes negative in a small filling range around ν = 0.7. This occurs in the region where the electron compressibility reaches its maximum, and a steep increase in ν_f vs ν is observed. This result reflects that the *f*-orbitals indeed dominate the low-energy physics of the minimal-TB model as they constitute up to 95% of the flat bands.

Data availability

The data supporting the findings in this work are publicly available online at https://doi.org/10.5281/zenodo.17066806.

References

1. Chang, C.-Z. et al. Experimental observation of the quantum anomalous Hall effect in a magnetic topological insulator. *Science* **340**, 167–170 (2013).
2. Deng, Y. et al. Quantum anomalous Hall effect in intrinsic magnetic topological insulator MnBi2Te4. *Science* **367**, 895–900 (2020).
3. Chen, G. et al. Tunable correlated Chern insulator and ferromagnetism in a moiré superlattice. *Nature* **579**, 56–61 (2020).
4. Serlin, M. et al. Intrinsic quantized anomalous Hall effect in a moiré heterostructure. *Science* **367**, 900–903 (2020).
5. Li, T. et al. Quantum anomalous Hall effect from intertwined moiré bands. *Nature* **600**, 641–646 (2021).
6. Park, H. et al. Observation of fractionally quantized anomalous Hall effect. *Nature* **622**, 74–79 (2023).
7. Xu, F. et al. Observation of integer and fractional quantum anomalous hall effects in twisted bilayer $MoTe_2$. *Phys. Rev. X* **13**, 031037 (2023).
8. Han, T. et al. Large quantum anomalous hall effect in spin-orbit proximitized rhombohedral. *Graphene* **651**, 647–651 (2023).
9. Lu, Z. et al. Fractional quantum anomalous Hall effect in multilayer graphene. *Nature* **626**, 759–764 (2024).
10. Chang, C.-Z., Liu, C.-X. & MacDonald, A. H. Colloquium: quantum anomalous Hall effect. *Rev. Mod. Phys.* **95**, 011002 (2023).
11. Ovchinnikov, D. et al. Intertwined topological and magnetic orders in atomically thin Chern insulator $MnBi_2Te_4$. *Nano Lett.* **21**, 2544–2550 (2021).
12. Chong, S. K. et al. Exchange-driven Chern states in high-mobility intrinsic magnetic topological insulators. *Phys. Rev. Lett.* **132**, 146601 (2024).
13. Choi, Y. et al. Correlation-driven topological phases in magic-angle twisted bilayer graphene. *Nature* **589**, 536–541 (2021).
14. Das, I. et al. Symmetry-broken Chern insulators and Rashba-like Landau-level crossings in magic-angle bilayer graphene. *Nat. Phys.* **17**, 710–714 (2021).
15. Nuckolls, K. P. et al. Strongly correlated Chern insulators in magic-angle twisted bilayer graphene. *Nature* **588**, 610–615 (2020).
16. Pierce, A. T. et al. Unconventional sequence of correlated Chern insulators in magic-angle twisted bilayer graphene. *Nat. Phys.* **17**, 1210–1215 (2021).
17. Saito, Y. et al. Hofstadter subband ferromagnetism and symmetry-broken Chern insulators in twisted bilayer graphene. *Nat. Phys.* **17**, 478–481 (2021).
18. Wu, S., Zhang, Z., Watanabe, K., Taniguchi, T. & Andrei, E. Y. Chern insulators, van Hove singularities and topological flat bands in magic-angle twisted bilayer graphene. *Nat. Mater.* **20**, 488–494 (2021).
19. Park, J. M., Cao, Y., Watanabe, K., Taniguchi, T. & Jarillo-Herrero, P. Flavour Hund's coupling, Chern gaps and charge diffusivity in moiré graphene. *Nature* **592**, 43–48 (2021).
20. Yu, J. et al. Correlated Hofstadter spectrum and flavour phase diagram in magic-angle twisted bilayer graphene. *Nat. Phys.* **18**, 825–831 (2022).
21. Polski, R. et al. Hierarchy of symmetry breaking correlated phases in twisted bilayer graphene. arXiv https://doi.org/10.48550/arXiv.2205.05225 (2022).
22. Tomarken, S. L. et al. Electronic compressibility of magic-angle graphene superlattices. *Phys. Rev. Lett.* **123**, 046601 (2019).
23. Sha, Y. et al. Observation of a Chern insulator in crystalline ABCA-tetralayer graphene with spin-orbit coupling. *Science* **384**, 414–419 (2024).
24. Han, T. et al. Correlated insulator and Chern insulators in pentalayer rhombohedral-stacked graphene. *Nat. Nanotechnol.* **19**, 181–187 (2024).
25. Spanton, E. M. et al. Observation of fractional Chern insulators in a van der Waals heterostructure. *Science* **360**, 62–66 (2018).
26. Lee, P. A., Nagaosa, N. & Wen, X. G. Doping a Mott insulator: physics of high-temperature superconductivity. *Rev. Mod. Phys.* **78**, 17–85 (2006).
27. Keimer, B., Kivelson, S. A., Norman, M. R., Uchida, S. & Zaanen, J. From quantum matter to high-temperature superconductivity in copper oxides. *Nature* **518**, 179–186 (2015).
28. Cao, Y. et al. Unconventional superconductivity in magic-angle graphene superlattices. *Nature* **556**, 43–50 (2018).
29. Cao, Y. et al. Correlated insulator behaviour at half-filling in magic-angle graphene superlattices. *Nature* **556**, 80–84 (2018).
30. Andrei, E. Y. & MacDonald, A. H. Graphene bilayers with a twist. *Nat. Mater.* **19**, 1265–1275 (2020).
31. Nuckolls, K. P. & Yazdani, A. A microscopic perspective on moire materials. *Nat. Rev. Mater.* **9**, 460–480 (2024).
32. Zondiner, U. et al. Cascade of phase transitions and Dirac revivals in magic-angle graphene. *Nature* **582**, 203–208 (2020).
33. Wong, D. et al. Cascade of electronic transitions in magic-angle twisted bilayer graphene. *Nature* **582**, 198–202 (2020).
34. Saito, Y. et al. Isospin Pomeranchuk effect in twisted bilayer graphene. *Nature* **592**, 220–224 (2021).
35. Rozen, A. et al. Entropic evidence for a Pomeranchuk effect in magic-angle graphene. *Nature* **592**, 214–219 (2021).
36. Datta, A., Calderón, M. J., Camjayi, A. & Bascones, E. Heavy quasiparticles and cascades without symmetry breaking in twisted bilayer graphene. *Nat. Commun.* **14**, 5036 (2023).
37. Xu, Y. et al. Correlated insulating states at fractional fillings of moiré superlattices. *Nature* **587**, 214–218 (2020).
38. Xu, Y. et al. Creation of moiré bands in a monolayer semiconductor by spatially periodic dielectric screening. *Nat. Mater.* **20**, 645–649 (2021).
39. Hu, Q. et al. Observation of Rydberg moiré excitons. *Science* **380**, 1367–1372 (2023).
40. Song, Z. D. & Bernevig, B. A. Magic-angle twisted bilayer graphene as a topological heavy fermion problem. *Phys. Rev. Lett.* **129**, 047601 (2022).

41. Shi, H. & Dai, X. Heavy-fermion representation for twisted bilayer graphene systems. *Phys. Rev. B* **106**, 245129 (2022).
42. Rai, G. et al. Dynamical correlations and order in magic-angle twisted bilayer graphene. *Phys. Rev. X* **14**, 031045 (2024).
43. He, M. et al. Dynamically tunable moiré exciton Rydberg states in a monolayer semiconductor on twisted bilayer graphene. *Nat. Mater.* **23**, 224–229 (2024).
44. Liu, J. & Dai, X. Orbital magnetic states in moiré graphene systems. *Nat. Rev. Phys.* **3**, 367–382 (2021).
45. Kerelsky, A. et al. Maximized electron interactions at the magic angle in twisted bilayer graphene. *Nature* **572**, 95–100 (2019).
46. Stepanov, P. et al. Competing zero-field Chern insulators in superconducting twisted bilayer graphene. *Phys. Rev. Lett.* **127**, 197701 (2021).
47. Lian, B. et al. Twisted bilayer graphene. IV Exact insulator ground states and phase diagram. *Phys. Rev. B* **103**, 205414 (2021).
48. Liu, J., Liu, J. & Dai, X. Pseudo Landau level representation of twisted bilayer graphene: band topology and implications on the correlated insulating phase. *Phys. Rev. B* **99**, 155415 (2019).
49. Peng, S., Weng, H. & Dai, X. RTGW2020: an efficient implementation of the multi-orbital Gutzwiller method with general local interactions. *Comput. Phys. Commun.* **276**, 108348 (2022).
50. Wang, L. et al. One-dimensional electrical contact to a two-dimensional material. *Science* **342**, 614–617 (2013).
51. Kim, K. et al. van der Waals heterostructures with high accuracy rotational alignment. *Nano Lett.* **16**, 1989–1995 (2016).
52. Carr, S. et al. Derivation of Wannier orbitals and minimal-basis tight-binding Hamiltonians for twisted bilayer graphene: first-principles approach. *Phys. Rev. Res.* **1**, 033072 (2019).
53. Bünemann, J. et al. Multiband Gutzwiller wave functions for general on-site interactions. *Phys. Rev. B* **57**, 6896–6916 (1998).
54. Lanatà, N. et al. Efficient implementation of the Gutzwiller variational method. *Phys. Rev. B* **85**, 035133 (2012).
55. Metzner, W. & Vollhardt, D. Ground-state properties of correlated fermions: exact analytic results for the Gutzwiller wave function. *Phys. Rev. Lett.* **59**, 121–124 (1987).

Acknowledgements

This work is supported by the National Key R&D Program of China (Grant No. 2021YFA1401300), the National Natural Science Foundation of China (Grant Nos. 92476108 and 12174439), and the Innovation Program for Quantum Science and Technology (Grants Nos. 2021ZD0302400 and 2021ZD0302300). X. Dai is supported by a fellowship and a CRF award from the Research Grants Council of the Hong Kong Special Administrative Region, China (Projects No. HKUST SRFS2324-6S01 and No. C7037-22GF) and by New Cornerstone Science Foundation.

Author contributions

Q.H., X.D. and Y.X. conceived the project. Q.H. fabricated the devices, performed the measurements, and analyzed the data. X.L. assisted with device fabrication. X.D. proposed the key theoretical insights. S.L. and H.S. carried out theoretical calculations under the supervision of X.D. Q.H., S.L., X.D. and Y.X. co-wrote the manuscript. All authors discussed the results and commented on the manuscript.

Competing interests

The authors declare no competing interests.

Additional information

Supplementary information The online version contains supplementary material available at https://doi.org/10.1038/s41467-025-64520-w.

Correspondence and requests for materials should be addressed to Xi Dai or Yang Xu.

Peer review information *Nature Communications* thanks Erfu Liu, and the other, anonymous, reviewer(s) for their contribution to the peer review of this work. A peer review file is available.